

PHOTOMETRIC AND SPECTRAL SIGNATURES OF 3D MODELS OF TRANSITING GIANT EXOPLANETS

A. BURROWS^{1,2}, E. RAUSCHER^{3,2}, D.S. SPIEGEL^{1,2}, & K. MENOU^{3,2}

Accepted to Ap.J. June 14, 2010

ABSTRACT

Using a 3D GCM, we create dynamical model atmospheres of a representative transiting giant exoplanet, HD 209458b. We post-process these atmospheres with an opacity code to obtain transit radius spectra during the primary transit. Using a spectral atmosphere code, we integrate over the face of the planet seen by an observer at various orbital phases and calculate light curves as a function of wavelength and for different photometric bands. The products of this study are generic predictions for the phase variations of a zero-eccentricity giant planet’s transit spectrum and of its light curves. We find that for these models the temporal variations in all quantities and the ingress/egress contrasts in the transit radii are small (< 1.0%). Moreover, we determine that the day/night contrasts and phase shifts of the brightness peaks relative to the ephemeris are functions of photometric band. The *J*, *H*, and *K* bands are shifted most, while the IRAC bands are shifted least. Therefore, we verify that the magnitude of the downwind shift in the planetary “hot spot” due to equatorial winds is strongly wavelength-dependent. The phase and wavelength dependence of light curves, and the associated day/night contrasts, can be used to constrain the circulation regime of irradiated giant planets and to probe different pressure levels of a hot Jupiter atmosphere. We posit that though our calculations focus on models of HD 209458b similar calculations for other transiting hot Jupiters in low-eccentricity orbits should yield transit spectra and light curves of a similar character.

Subject headings: stars: individual (HD 209458)—(stars:) planetary systems—planets and satellites: general

1. INTRODUCTION

Circa April 2010, more than 70 exoplanets had been discovered transiting their primary stars⁴. Transits are useful in the characterization of exoplanets because they break the the mass/orbital-inclination degeneracy of radial-velocity measurements. Moreover, a planet’s radius can be directly measured, yielding mass (M_p) and radius (R_p) correlations with which theorists can extract useful information about bulk composition and structure and can attempt to fit radius evolution models (Guillot et al. 1996; Burrows et al. 2000; Brown et al. 2001; Hubbard et al. 2001; Baraffe et al. 2003; Chabrier et al. 2004; Charbonneau et al. 2007).

However, since atmospheric opacity is a function of wavelength, a planet’s transit radius is also a function of wavelength (Seager & Sasselov 2000; Brown 2001; Spiegel et al. 2007; Fortney et al. 2003,2010). The variation with wavelength in the measured radius (actually an impact parameter) provides an ersatz spectrum directly related to the planet’s atmospheric composition near the terminator. This radius spectrum, unlike the planet’s spectrum at secondary eclipse, is more dependent upon composition than upon the temperature profile, and so

provides complementary information to a planet’s own direct emissions. The latter can be measured during secondary eclipse, but also during the traverse by the planet of its orbit as it traces out its phase light curve.

The transit radius spectrum and the planet emission spectrum as a function of phase can, therefore, together help constrain planet properties (Fortney et al. 2006,2010). However, the stellar irradiation of such an exoplanet severely breaks what would otherwise be quasi-spherical symmetry, producing large day-night contrasts in thermal structure, zonal flows and banding, and violent atmospheric dynamics (Showman & Guillot 2002; Guillot & Showman 2002; Cho et al. 2003,2008; Burkert et al. 2005; Cooper & Showman 2005,2006; Showman et al. 2008,2009; Showman, Cho, & Menou 2010; Dobbs-Dixon & Lin 2008; Dobbs-Dixon, Cumming, & Lin 2010; Rauscher et al. 2007,2008; Menou & Rauscher 2009; Rauscher & Menou 2010). Importantly, such behavior may have photometric and spectral signatures. It is the exploration of such signatures that motivates this paper. The state-of-the-art in the 3D modeling of exoplanet atmospheres is still evolving and has not yet reached a level of maturity where detailed predictions for each known exoplanet are robust. Hence, in this paper we focus on a few generic ideas and conjectures that emerge from our modeling efforts. The procedure we have pursued is the following: First, using a 3D general circulation model (GCM) we derive dynamic model atmospheres at various epochs after they have achieved a steady state. Second, we post-process these 3D model atmospheres with a spectral atmosphere code to obtain transit radius spectra at various epochs during ingress, egress, and total transit. We assume equilibrium molecular compositions and solar metallicity. Third, using the

¹ Department of Astrophysical Sciences, Peyton Hall, Princeton University, Princeton, NJ 08544; burrows@astro.princeton.edu, dsp@astro.princeton.edu

² Kavli Institute for Theoretical Physics, University of California, Santa Barbara, CA 93106

³ Department of Astronomy, Columbia University, 550 West 120th Street, New York, NY 10027; emily@astro.columbia.edu, kristen@astro.columbia.edu

⁴ see J. Schneider’s Extrasolar Planet Encyclopaedia at <http://exoplanet.eu>, the Geneva Search Programme at <http://exoplanets.eu>, and the Carnegie/California compilation at <http://exoplanets.org>

same 3D model atmosphere, we integrate over the “visible” disk and calculate phase light curves as a function of wavelength and for various standard photometric bands. The results are generic predictions which, though not expected to be quantitatively precise and constraining on any particular giant exoplanet, nevertheless contain qualitatively interesting features that should inform future measurements. For specificity, we focus on two models of HD 209458b (Charbonneau et al. 2000; Henry et al. 2000), one with and one without an “extra absorber” and a thermal inversion (Hubeny, Burrows, & Sudarsky 2003; Burrows et al. 2007; Fortney et al. 2008; Spiegel et al. 2009; Knutson et al. 2008), but suggest our qualitative results are generic beyond this planet and this modeling paradigm (see also Fortney et al. 2006, 2010).

In §2, we summarize our methodology and techniques. Then, in §3 we describe the 3D models and various of their salient characteristics. We go on in §4 to present our results for the wavelength-dependent transit radius and ingress-egress asymmetries and in §5 we turn to a full discussion of the derived light curves. This section contains not only wavelength-dependent planet-star flux ratios as a function of phase, but the phase variation of several photometric planet band fluxes. In §6, we summarize our general conclusions.

2. METHODOLOGY

2.1. 3D GCM Models

We use the same modified version of the University of Reading’s Intermediate General Circulation Model (Hoskins & Simmons 1975) as presented in Menou & Rauscher (2009) and Rauscher & Menou (2010), where a detailed description of the numerical implementation can be found. We use a horizontal spectral resolution of T31, roughly equivalent to a 4° resolution on the sphere, and 45 vertical levels which are logarithmically spaced in pressure from 100 bar to 10 microbar. We employ a simplified Newtonian relaxation scheme for the radiative forcing, so that everywhere the atmosphere heats or cools toward a prescribed three-dimensional equilibrium temperature profile, on some representative radiative timescale (Iro, Bézard, & Guillot 2005). The equilibrium temperature profiles are chosen to have a horizontal dependence such that on the dayside the fourth power of the equilibrium temperature goes linearly with the cosine of the angle from the substellar point and on the nightside it is constant. The amplitude of the temperature difference between the substellar point and the nightside is taken from 1D radiative transfer models (Burrows et al. 2008; see Fig. 1), as are the dependences with pressure and depth of the equilibrium temperatures needed in the Newtonian scheme.

Our choice for the angular dependence of the dayside equilibrium temperatures is loosely motivated by the fact that the equilibrium black body temperature (T_{eq}) of an irradiated surface at a slant angle is determined by setting the incident flux on the angled surface equal to the emitted flux and by the σT_{eq}^4 dependence of the latter. We scale the entire vertical profile of internal equilibrium temperatures to which the Newtonian cooling scheme is dynamically driving the actual temperature by this same angular factor. In this way, the expectation that the annuli on the planet away from the substellar point will

be heated less by the star than the gas at the substellar point is realized. For the night side, which by definition is not irradiated by the star, we employ the simplifying assumption that in equilibrium without night-side dynamics the planet would resemble more an isolated brown dwarf with uniform emission and profiles. Note that these assumptions about the solid-angle distribution of the equilibrium temperature profiles still allow the 3D GCM dynamics to redistribute heat in all regions of the planet’s atmosphere and that the actual temperatures perforce deviate from these equilibrium temperatures due to such advection, sometimes to a significant degree. However, clearly our ansatz could be improved by doing the 3D radiative transfer that the problem will eventually demand. For now, we believe our approach allows us to capture the essence, if not the detail, of the thermal character of the dynamical atmospheres we are studying.

Thus, the only difference between the inputs for our two 3D GCM models of HD 209458b is the different 1D profiles of the substellar equilibrium temperatures, where one was calculated including an extra absorber high in the atmosphere and one was calculated without. The radiative timescales are constant on a given pressure level and they increase with pressure at depth. They are taken from the profile in Iro et al. (2005), except for the deepest model levels. Figure 1 provides a detailed profile of the radiative times adopted. All other planetary and numerical parameters match those described in Rauscher & Menou (2010). Each model was run for 500 planetary days (\equiv orbits), after which a statistically steady state has been reached for all levels at pressures less than 1 bar. Levels deeper than this are not directly probed by the types of observations considered here. To summarize, the key differences between the present models and those in Rauscher & Menou (2010) are (i) the different relaxation temperature profiles used and (ii) the greater vertical extent of pressures modeled, up to 10 microbar in the present study.

2.2. Method for Deriving Transit Curves and Their Wavelength Dependence

To calculate the spectrum of the transit radius, we create a data cube in latitude, longitude, and altitude of the temperatures, densities, and pressures of one of the 3D GCM models described in §2.1. At a given wavelength, using the snapshot at day 500 in a 500-day model, we cast 200 rays through an annulus at a given impact parameter and calculate the optical depth (τ_λ) along the chord. The minuscule index of refraction effects (Fortney et al. 2003) are ignored. We use the opacity database described in Sharp & Burrows (2007) and equilibrium chemical abundances taken from Burrows & Sharp (1999) and Burrows et al. (2001). Solar abundances were assumed, and we have used the inclination angle of 86.6° suitable for HD 209458b. The differential area of the annulus associated with a given ray is then weighted by the quantity $1 - e^{-\tau}$. A new impact parameter is then chosen and the process is repeated. By this means, the total effective area of the atmosphere at a given wavelength is obtained. It is this effective area that determines the magnitude of the occultation by the planet of the star due to the atmosphere. Since there is no core nor structural information in the atmospheric GCM, we assume that the baseline planet

radius is the radius measured for HD 209458b in the optical by Knutson et al. 2007 ($1.32 R_J$) and shift the differential area for a given wavelength calculated as described above by the average of the corresponding calculation in the 0.5 to 0.7 μm wavelength region, rendering the average differential area in the 0.5 to 0.7 μm wavelength region zero. Other procedures can be followed, but all of them are equivalent to first order in the (small) differential area, where only the first-order term is relevant. When the transit is partial (during ingress and egress), we use the formalism of Mandel & Agol (2002) to determine planet-star intercept angles as a function of orbital phase, between which the calculations of the total relevant area of the atmosphere are performed. Since the planet is assumed to be in synchronous rotation, it will rotate with the orbit during transit. This effect, which can amount to a 10-20° turn and which slightly changes the regions of the atmosphere intercepted by the cast rays included in the optical depth calculation, is incorporated in the formalism. We perform such calculations for 2000 frequencies from 0.4 μm to 30 μm and 200 phase angles from just before ingress to just after egress.

Though we performed some transit calculations at other days (e.g., days 451, 476, 496) in the 500-day runs, we found little variation (less than 0.5%) in the results. Hence, we focused on only the day-500 3D GCM models for the two input models, one with an extra absorber and one without, as described in §2.1. Note that such a small temporal variation justifies the use of a single snapshot for both these transit radius calculations and the phase light curves calculations described below.

2.3. Spectral Post-Processing to Derive Wavelength-Dependent Light Curves

To obtain the total planetary photon fluxes as a function of wavelength, we use the code COOLTLUSTY (Hubeny 1988; Hubeny & Lanz 1995; Burrows, Sudarksy, & Hubeny 2003; Burrows et al. 2008). This code incorporates the same composition and opacity algorithms we employ to perform the transit spectrum calculations described in §2.2. First, we divide the surface seen by the observer at a given phase angle into about 2000 patches. Then, we cast a ray from the observer to the patch and into the planet at the associated slant angle. The densities, temperatures, and pressures at that slant angle are then used to calculate the instantaneous radiation field emerging from the patch (without allowing the code to seek radiative equilibrium and ignoring the time-dependent term in the transport equation). That intensity is then multiplied by the projected area of the patch and all the patches seen by the observer at that phase angle were added. This is done for 1000 frequency points from 0.4 μm to 30 μm . We also calculated the associated photometric colors in 24 bands, 9 of which we report here. The stellar flux is multiplied by the angle of incidence on the patch with respect to the star and a Kurucz (1994) model for HD 209458 is employed. The stellar flux is necessary to handle the Rayleigh scattered component and to obtain the planet/star flux ratio. We remind the reader that the 3D GCM model (Rauscher & Menou 2010) is calculated using Newtonian cooling and not with radiative transfer, so there are inconsistencies in our general approach. However, our focus here is on the character of generic results (for instance for differ-

ent photometric bands and given general characteristics of the 3D flow), and not on specific predictions for HD 209458b.

3. DESCRIPTION OF THE 3D GCM MODELS

Although the relaxation temperature profiles are very different for our two atmospheric models with and without a high-altitude absorber (Fig. 1), we nevertheless find that these models have rather similar flow patterns. This is perhaps even more striking since these circulation patterns are also qualitatively similar to that described in Rauscher & Menou (2010), which has a rather different temperature relaxation profile. This suggests that the circulation pattern studied here is more strongly governed by the choice of the T^4 -behaves-linearly-with- $\cos\theta$ horizontal dependence than by the amplitude or the detailed vertical structure of the relaxation temperature profile adopted. This supports the notion that the main qualitative results shown in the present study may be extended to other close-in giant planets.

While details differ, key flow features are common to both model atmospheres: transonic wind speeds, with peak wind speeds of 10 and 20 km s^{-1} high up in the models with and without an extra absorber, respectively; a super-rotating (eastward) equatorial jet that extends across many pressure scale heights (see Fig. 2); a pronounced chevron-shaped shock-like feature at a longitude of $\sim 135^\circ$ at intermediate pressure levels; and large stationary vortices in each hemisphere that extend almost from the equator to the poles and are centered at a longitude of $\sim 120^\circ$ (Rauscher & Menou 2010). High in the atmosphere, where heat advection is not dominant, the day-night temperature difference is greater in the model run with an extra absorber because of the stronger forcing profile adopted. In both models, the horizontal temperature field is close to equilibrium, with a hot dayside and a cold nightside at pressures less than 1 mbar. The hottest atmospheric region is advected eastward by $\sim 45^\circ$ at the 100 mbar level and by $\sim 90^\circ$ at the 1 bar level, while the temperature field is fairly well longitudinally homogenized at deeper pressure levels.

The general trend in these models is to have the hottest atmospheric regions advected farther away from the substellar point at deeper pressure levels, with potentially observable consequences as discussed in §5.2. For the model with the extra absorber, however, there is an additional complication. Although both models show localized heating where a shock-like feature develops in the flow, this heating is significantly more pronounced in the model with absorber. We attribute this difference to faster winds driven by a stronger day-night forcing in the model with absorber. This, rather than direct heat advection from the dayside, determines the location of the hottest atmospheric region at pressure levels 15-45 mbar in the model with absorber. As a result, the peak temperature region at these levels does not simply transition away from the substellar point gradually with depth, but it is significantly affected by a systematic shift to $\sim 135^\circ$, where the shock-like feature is located.⁵

Figure 3 depicts temperature maps with and without

⁵ It is worth recalling that there are modeling concerns regarding this type of shock-like features, as discussed in more detail by Goodman (2009) and Rauscher & Menou (2010).

dynamical redistribution and with and without an extra optical absorber. To emphasize the contrasts, the atmospheric scale heights are exaggerated by a factor of ten. The longitudinal flows distribute heat to the nightside, and thereby partially even out the scale height bulge differential between the dayside and nightside. Additionally, Figs. 4 depict the distribution of methane (CH_4) at a pressure level of 5.7 millibars, if in chemical equilibrium, over the surface of our 3D GCM models of HD 209458b, with and without an extra high-altitude optical absorber. If not in methane, carbon would reside in carbon monoxide in these models, which predominates on the day sides (particularly, in this model set, for the model with the extra optical absorber). In the model without the extra optical absorber, we note the presence of the tongue of methane-depleted (CO-rich) material dragged from the dayside to the nightside in the equatorial belt (see also Cooper & Showman 2006). The degree of such advection is a function of vertical height/pressure level. In principle this feature could be detected in a precision comparison of the ingress and egress transit spectra (Fortney et al. 2010). However, we find, as did Fortney et al. (2010), that this differential effect can be quite small, less than one percent of the already small variation with wavelength expected for the transit radius. Be that as it may, these two figures partially represent the model context in which we have performed our post-processing exercise.

4. THE WAVELENGTH-DEPENDENCE OF THE TRANSIT RADIUS

The top panel of Fig. 5 shows the normalized fractional area of the atmosphere occulting the star as a function of wavelength as the planet enters and leaves transit for the model without an extra optical absorber at altitude. The fractions are all normalized to the instantaneous average value in the optical wavelength range from 0.5 to 0.7 microns. Hence, the average value of this fraction in that wavelength range (“optical”) is zero. For this model, the base position in the atmosphere where the chord optical depth is of order unity for optical photons (which defines the transit radius) is deep inside the atmosphere (near 0.1 bars). The bottom panel of Fig. 5 is the same as the top panel, but for the model with the extra absorber at altitude. The action of the extra absorber is clearly seen in the optical region, and the normalization is as performed for the top panel. However, for this model the chord optical depth is of order unity for a base pressure near a millibar, much higher in the atmosphere than for the model without the extra absorber. This difference results in perceptible differences between the two classes of models.

Water is ubiquitous in our planet model atmospheres and its features dominate these spectra. For our models, the egress and ingress are rather symmetrical, differing by no more than $\sim 0.8\%$ at any wavelength, due predominantly to slight differences in the scale heights near the respective terminators. These small ingress/egress differences are most prominent in the water bands, but there are slight differential signatures in the methane and carbon monoxide bands at $\sim 1.6 \mu\text{m}$ and $\sim 3.3 \mu\text{m}$ and at $\sim 2.3 \mu\text{m}$ and $\sim 4.6 \mu\text{m}$, respectively, as might be expected from the advection of gas across the terminator depicted in Figs. 4.

Figure 6 compares the transit radii during full transit as a function of wavelength for both models depicted in Fig. 5. The normalization for both models is to the measured radius in the optical ($\sim 1.32 R_J$; Knutson et al. 2007). We believe this to be the most physically and observationally sensible normalization. Note that when so normalized the two models, which differ only in whether there is an extra optical absorber at altitude, predict very different radii, though the relative differences when comparing radii at different wavelengths outside the optical are similar. Therefore, comparing the radius as inferred from optical observations to that inferred from infrared observations is diagnostic of the presence of an extra absorber. Unfortunately, the infrared transit radius data are not consistent with either the extra-absorber model or the no-extra-absorber model. A comparison with the *Spitzer*/IRAC data from Beaulieu et al. (2010) and the 24-micron MIPS data from Richardson et al. (2006) suggests that neither model fits both sets of data simultaneously, but a major discrepancy is also the wide spread between IRAC 3/4 and IRAC 1/2. The same discrepancy between model and data was noted by Fortney et al. (2010) for their models and is as yet unexplained.

Our implementation of the extra absorber puts it throughout the upper atmosphere, at the lowest pressures. Given this, and as Fig. 6 demonstrates, the corresponding model does not evince much contrast in and out of the Na-D doublet. This is in contradiction with the observations of Charbonneau et al. (2002) and may hint at an upper boundary to the extent of the optical absorber (if it exists) if the Na-D data are to be accommodated.

5. LIGHT CURVES

The planet fluxes themselves, and their phase variation, should speak volumes about the atmospheres of hot Jupiters, in particular their thermal and compositional profiles and the longitudinal dependence of their circulation regimes (Cowan & Agol 2008). Using the methodologies described in §2.3, we now present results for the planet-star flux ratios and photometric variations for our two models of HD 209458b as it traverses its orbit.

5.1. *Planet-Star Flux Ratio as a Function of Wavelength and Phase*

Figure 7 portrays the planet-star flux ratios versus wavelength, for the models with and without the extra optical absorber and as a function of phase in the planet’s (HD 209458b’s) orbit. Here, zero phase is at secondary eclipse. Superposed are various data sets and the corresponding “1D” spectral models using the method of Burrows et al. (2007,2008). The slight differences between the zero-phase 3D calculations and the “1D” predictions are due to the different methods of determining the average effect of emission from the day-side hemisphere and to the dynamics inherent in 3D models. We note many things about these curves. First, the data points at secondary eclipse are much more consistent with the zero-phase prediction(s) for the model with an extra absorber. This was pointed out in Burrows et al. (2007) and Knutson et al. (2008). Second, the variation with phase from the dayside to the nightside is much larger for the model with an extra absorber and inversion. This

is a generic feature of predictions with strong optical absorption at altitude on the dayside. Third, there are interesting differences in the phase-dependence at different wavelengths. The variations longward of ~ 15 microns are generally largest. The variation at ~ 10 microns is muted. The water feature near ~ 6.2 microns becomes relatively more prominent on the nightside, while modest on the dayside. The phase variation near ~ 4 microns is slight. The phase variation from ~ 8 to ~ 10 microns is much larger for the hot day-side model with the extra absorber. In sum, there are important variations in infrared colors with orbital phase that may be diagnostic of the atmosphere models.

The planet-star flux ratios depicted in Figs. 7 are integrals over the surface of the planet of brightness maps such as are shown in Figs. 8. The associated panels in Fig 8 are representative planet brightness maps in the IRAC 3 band, the *I* band, and the *J* band, the latter for the models with and without the extra absorber. All the maps are at full phase (secondary eclipse). In principle, these are what the planet HD 209458b would look like in “glasses” for the various bands, given the various relative color maps. The color mappings depict the magnitude difference between the brightest point on the planet and are different for each given rendering and band. Note that the hot spot in each band is shifted by a different angle relative to the substellar point, reflecting the different approximate “photospheric” pressures of the various bands and the variation in the degree and strength of zonal heat advection with depth (Showman et al. 2009). In particular, the IRAC band fluxes, formed as they are at altitude, are shifted the least, by no more than $\sim 20^\circ$ but mostly close to $\sim 0^\circ$. These differential phase shifts are useful diagnostics of the zonal flow regimes and models (Cowan & Agol 2008).

5.2. Phase Dependence of the Photometric Band Fluxes

This is particularly clear from Fig. 9, which depicts for the two different atmosphere models and for our fiducial HD 209458b assumptions integrated relative light curves versus orbital phase in the *R*, *I*, *J*, *H*, *K*, IRAC 1, IRAC 2, IRAC 3, and IRAC 4 bands. These data are derived by integrating maps such as are shown in Figs. 8. The different phase shifts of the hot spots suggested in Figs. 8 are manifest in these plots. While the shifts in the IRAC bands are smallest (generally being formed at altitude at lower pressures), the shift in IRAC 1 being the largest among these ($\sim 20^\circ$ for the no-absorber model and $\sim 10^\circ$ for the absorber model), for the model with no extra absorber the shifts in the *I* and *J* bands can be $\sim 40^\circ$ and $\sim 45^\circ$, respectively. For the absorber model, the shift in the *J* band is comparable, while the shift in the *I* band is only $\sim 10^\circ$. The fact that many of the curves are not flat on the far right of these plots near 180° is another indication of the skews in the phase light curves and of the (differential) dynamical advection of heat by planetary zonal winds.

Ignoring the IRAC bands, the contrasts are generally largest for bands at the shortest wavelengths. In Fig. 9, the differences between the models with and without the high-altitude absorber are clear, with the brightness variations with phase being larger for the absorber model in the IRAC, *R*, and *I* bands. The two models are comparable in the near-infrared bands. The specific numbers

derived are not as important as the general trends revealed by this representative modeling exercise. In principle, by measuring such phase curves in different bands, one could back out information on the thermal and wind profiles as a function of depth and longitude. This is in part because the different bands are formed and have approximate photospheric positions at different pressures in the atmosphere. Such remote sensing of a hot Jupiter atmosphere would enable a new level of scrutiny for exoplanets and may be possible using JWST.

6. CONCLUSIONS

Using a 3D GCM with Newtonian cooling and day- and nightside equilibrium temperature profiles based on two 1D spectral models (with and without a thermal inversion and a hot upper atmosphere), we created dynamical models of the transiting giant exoplanet HD 209458b. We post-processed these 3D model atmospheres with a detailed opacity code to obtain transit radius spectra at various epochs during the primary transit. Then, using a spectral atmosphere code, we integrated over the face of the planet seen by an observer at various orbital phases and calculated light curves as a function of wavelength and for nine different photometric bands from *R* (~ 0.6 μm) through IRAC 4 (~ 8 μm). The products of this study are generic predictions for the character of the expected phase variations both of a giant planet’s transit spectrum and of its light curves. Since our GCM employed Newtonian cooling (and not radiative transfer using opacities that corresponded with those used in the post-processing), the calculations are slightly inconsistent. Nevertheless, the results have interesting features that should inform future measurements. We found that the temporal variations in the derived integral quantities for this model suite are small (less than 1%) and that the ingress/egress contrasts due to zonal flows, while also small ($< 0.5 - 1.0\%$), are most manifest due to the scale-height asymmetries near the terminators and in the water bands. While models we have generated with and without the methane and carbon monoxide bands indicate that ingress/egress differences in the CO and CH_4 bands might be diagnostic of both carbon chemistry and abundance asymmetries due to zonal flows near the terminators, the differential effects due to different carbon-species abundances at the different terminators are small (less than a few tenths of a percent). A similar conclusion was reached by Fortney et al. (2010), who nevertheless found a slightly larger quantitative effect.

Since the transit radius of HD 209458b has been measured in the optical, it should not be allowed to differ when comparing models with and without an upper-atmosphere absorber and the predicted radii at other wavelengths must be determined relative to it. When this is done, the predicted radii in the near- and mid-infrared are very different (by as much as $0.05 R_J$), though our current models do a poor job of fitting all the transit radius data for HD 209458b simultaneously (e.g., Knutson et al. 2007; Beaulieu et al. 2010; Richardson et al. 2006). The reason for this discrepancy is currently unknown.

We determined that the angular phase shifts of the brightness peaks relative to the orbital ephemeris are functions of photometric band. The *J*, *H*, and *K* bands are shifted most, by as much as $\sim 45^\circ$, while the IRAC bands are shifted least. This is because different bands

are spectrally formed at different pressure depths and the zonal winds that advect heat are depth-dependent. The IRAC band photospheres are generally at altitude, while those in the near infrared are at deeper pressures near and above ~ 0.1 bars. Therefore, the question of the magnitude of the downwind shift in the planetary “hot spot” due to equatorial winds is nuanced, depending upon the waveband in which measurements are made. This wavelength dependence of the phase shift in the brightness light curve, and the associated day/night contrasts, can in principle be used to constrain the circulation regimes of irradiated giant planets and to probe different pressure levels of a hot Jupiter atmosphere. Though our calculations focused on models of HD 209458b, similar calculations for other transiting hot Jupiters in low-eccentricity orbits should yield transit spectra and light curves of a similar character. As the subject of comparative exo-

planetology matures, and JWST comes online, such observational manifestations of global circulation may well become possible for a wide range of irradiated planets. Our models have been constructed to help prepare the way, however imperfectly, for that era.

We acknowledge useful conversations with Ian Dobbs-Dixon and Brad Hansen and Ivan Hubeny for his general support of the COOLTLUSTY code. AB was supported by NASA grant NNX07AG80G and under JPL/Spitzer Agreements 1328092, 1348668, and 1312647. ER was supported by a NASA Graduate Student Research Program Fellowship, contract NNX08AT35H, and KM was supported by the Spitzer Space Telescope Program under contract JPLCIT 1366188. The authors are pleased to note that part of this work was performed while in residence at the Kavli Institute for Theoretical Physics, funded by the NSF through grant no. PHY05-51164.

REFERENCES

Baraffe, I., Chabrier, G., Barman, T.S., Allard, F., & Hauschildt, P.H. 2003, *A&A*, 402, 701 Evolutionary models for cool brown dwarfs and extrasolar giant planets. The case of HD 209458

Beaulieu, J.P. et al. 2010, accepted to *MNRAS*, (arXiv:0909.0185)

Brown, T. M. 2001, *ApJ*, 553, 1006

Brown, T. M., Charbonneau, D., Gilliland, R.L., Noyes, R.W., & Burrows, A. 2001, *ApJ*, 552, 699

Burkert, A., Lin, D.N.C., Bodenheimer, P., Jones, C., & Yorke, H. 2005, *ApJ*, 618, 512

Burrows, A. & Sharp, C.M. 1999, *ApJ*, 512, 843

Burrows, A., Guillot, T., Hubbard, W.B., Marley, M.S., Saumon, D., Lunine, J.I., & Sudarsky, D. 2000, *ApJ*, 534, 97

Burrows, A., Hubbard, W.B., Lunine, J.I., & Liebert, J. 2001, *Rev. Mod. Phys.*, 73, 719

Burrows, A., Sudarsky, D. & Hubeny, I. 2006, *ApJ*, 650, 1140

Burrows, A., Hubeny, I., Budaj, J., Knutson, H.A., & Charbonneau, D. 2007, *ApJ*, 668, L171

Burrows, A., Budaj, J., & Hubeny, I. 2008, *ApJ*, 678, 1436

Burrows, A. & Orton, G. 2010, in *EXOPLANETS*, edited by S. Seager, to be published in the Spring of 2010 in the Space Science Series of the University of Arizona Press (Tucson, AZ) (refereed), (arXiv:0910.0248)

Chabrier, G., Barman, T., Baraffe, I., Allard, F., & Hauschildt, P.H. 2004, *ApJ*, 603, L53

Charbonneau, D., Brown, T. M., Latham, D. W., & Mayor, M. 2000, *ApJ*, 529, L45

Charbonneau, D., Brown, T. M., Noyes, R. W., & Gilliland, R. L. 2002, *ApJ*, 568, 377

Charbonneau, D., Brown, T.M., Burrows, A., & Laughlin, G. 2007, in “Protostars and Planets V,” ed. B. Reipurth and D. Jewitt, p. 701 (University of Arizona Press), astro-ph/0603376

Cho, J. Y.-K., Menou, K., Hansen, B. M. S., & Seager, S. 2003, *ApJ*, 587, L117

Cho, J. Y.-K., Menou, K., Hansen, B. M. S., & Seager, S. 2008, *ApJ*, 675, 817

Cooper, C.S. & Showman, A.P. 2005, *ApJ*, 629, L45

Cooper, C.S. & Showman, A.P. 2006, *ApJ*, 649, 1048

Cowan, N.B. & Agol, E. 2008, *ApJ*, 678, L129

Deming, D., Seager, S., Richardson, L.J., & Harrington, J., 2005, *Nature*, 434, 740

Dobbs-Dixon, I. & Lin, D.N.C. 2008, *ApJ*, 673, 513

Dobbs-Dixon, I., Cumming, A., & Lin, D.N.C. 2010, *ApJ*, 710, 1395

Fortney, J.J., Sudarsky, D., Hubeny, I., Cooper, C.S., Hubbard, W.B., Burrows, A., & Lunine, J.I. 2003, *ApJ*, 589, 615

Fortney, J.J., Cooper, C.S., Showman, A.P., Marley, M.S., & Freedman, R.S. 2005, *ApJ*, 652, 746

Fortney, J.J., Lodders, K., Marley, M.S., & Freedman, R.S. 2008, *ApJ*, 678, 1419

Fortney, J.J., Shabram, M., Showman, A.P., Lian, Y., Freedman, R.S., Marley, M.S., & Lewis, N.K. 2010, *ApJ*, 709, 1396

Guillot, T., Burrows, A., Hubbard, W. B., Lunine, J. I., & Saumon, D. 1996, *ApJ*, 459, 35

Guillot, T. & Showman, A.P. 2002, *A&A*, 385, 156

Henry, G., Marcy, G. W., Butler, R. P., & Vogt, S. S. 2000, *ApJ*, 529, L41

Hoskins, B.J. & Simmons, A.J. 1975, *Quart. J. R. Met. Soc.*, 101, 637

Hubbard, W.B., Fortney, J.F., Lunine, J.I., Burrows, A., Sudarsky, D., & Pinto, P.A. 2001, *ApJ*, 560, 413

Hubeny, I. 1988, *Comput. Phys. Commun.*, 52, 103

Hubeny, I. & Lanz, T. 1995, *ApJ*, 439, 875

Hubeny, I., Burrows, A., & Sudarsky, D. 2003, *ApJ*, 594, 1011

Iro, N., Bézard, B., & Guillot, T. 2005, *A&A*, 436, 719

Knutson, H., Charbonneau, D., Noyes, R.W., Brown, T.M., & Gilliland, R.L. 2007, *ApJ*, 655, 564

Knutson, H.A., Charbonneau, D., Allen, L.E., Burrows, A., & Megeath, S.T. 2008, *ApJ*, 673, 526

Kurucz, R. 1994, *Kurucz CD-ROM No. 19*, (Cambridge: Smithsonian Astrophysical Observatory)

Mandel, K. & Agol, E. 2002, *ApJ*, 580, L171

Menou, K. & Rauscher, E. 2009, *ApJ*, 700, 887

Rauscher, E., Menou, K., Cho, J.Y.-K., Seager, S., & Hansen, B.M.S. 2007, *ApJ*, 662, L115, arXiv:0712.2242

Rauscher, E., Menou, K., Cho, J.Y.-K., Seager, S., & Hansen, B.M.S. 2008, *ApJ*, 681, 1646

Rauscher, E. & Menou, K. 2010, *ApJ*, 714, 1334 (arXiv:0907.2692)

Richardson, L.J., Harrington, J., Seager, S., & Deming, D. 2006, *ApJ*, 649, 1043

Seager, S. & Sasselov, D. 2000, *ApJ*, 537, 916

Sharp, C.M. & Burrows, A. 2007, *ApJS*, 168, 140

Showman, A.P., Cho, J. Y.-K., & Menou, K. 2010, in *EXOPLANETS*, edited by S. Seager, to be published in the Spring of 2010 in the Space Science Series of the University of Arizona Press (Tucson, AZ) (arXiv:0911.3170)

Showman, A.P., Cooper, C.S., Fortney, J.J., & Marley, M.S. 2008, *ApJ*, 682, 559 (arXiv:0802.0327)

Showman, A.P., Fortney, J.J., Lian, Y., Marley, M.S., Freedman, R.S., Knutson, H.A., Charbonneau, D. 2009, *ApJ*, 699, 564

Showman, A. P. & Guillot, T. 2002, *A&A*, 385, 166

Spiegel, D. S., Haiman, Z., & Gaudi, B. S. 2007, *ApJ*, 669, 1324 (arXiv:0902.3995)

Swain, M., Tinetti, G., Vasisht, G., Deroo, P., Griffith, C., Bouwman, J., Chen, P., Burrows, A., Matthews, J., Rowe, J.F., Kuschnig, R., & Angerhausen, D. 2009, *ApJ*, 704, 1616

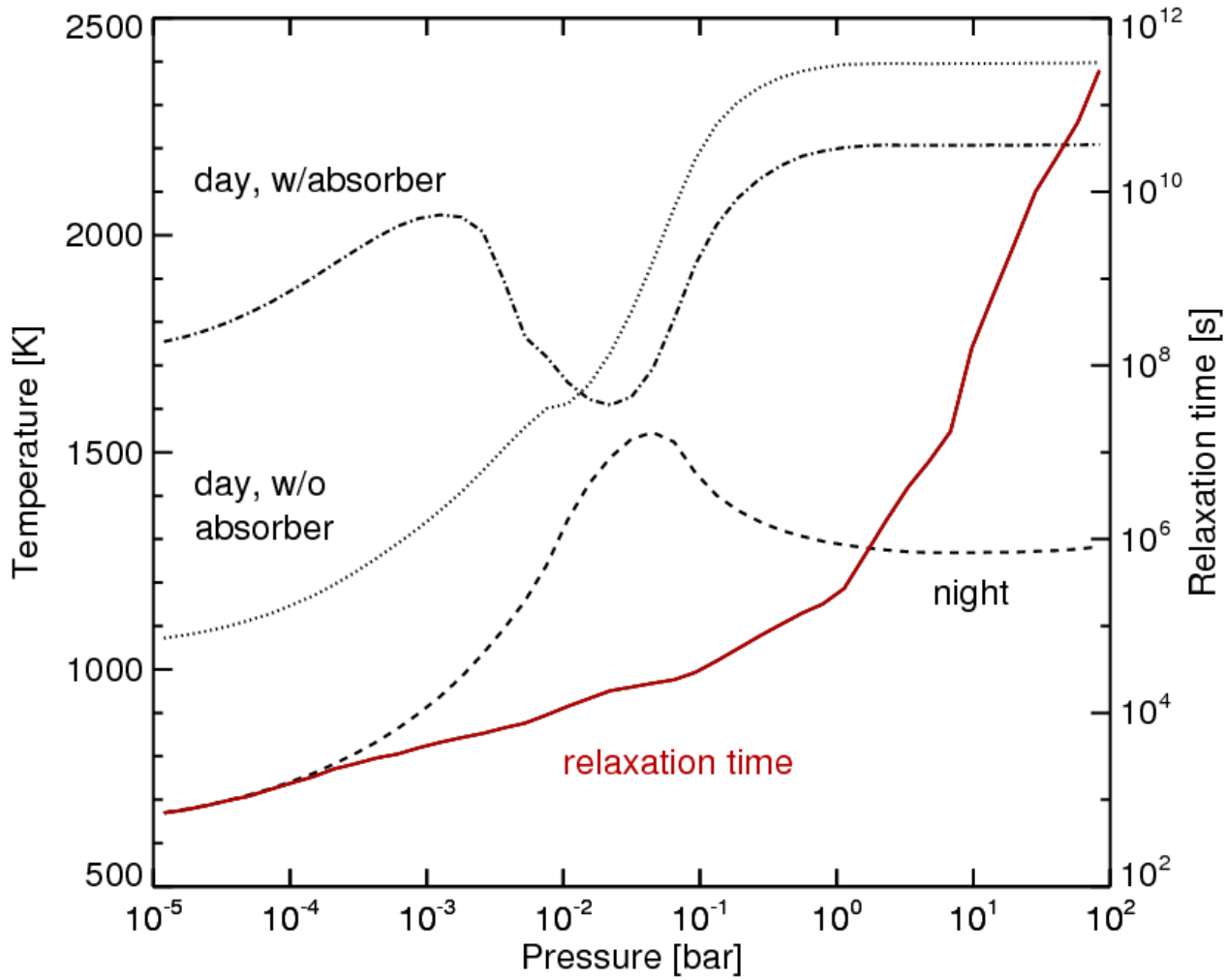


FIG. 1.— The relaxation temperature-pressure profiles used for the forcing. The night side profile (dashed) is the same for both models, with separate substellar point profiles for the models with (dot-dashed) and without (dotted) an extra absorber high in the atmosphere. The solid red line shows the relaxation times used at each pressure level, for both models. See text for a description of the forcing scheme.

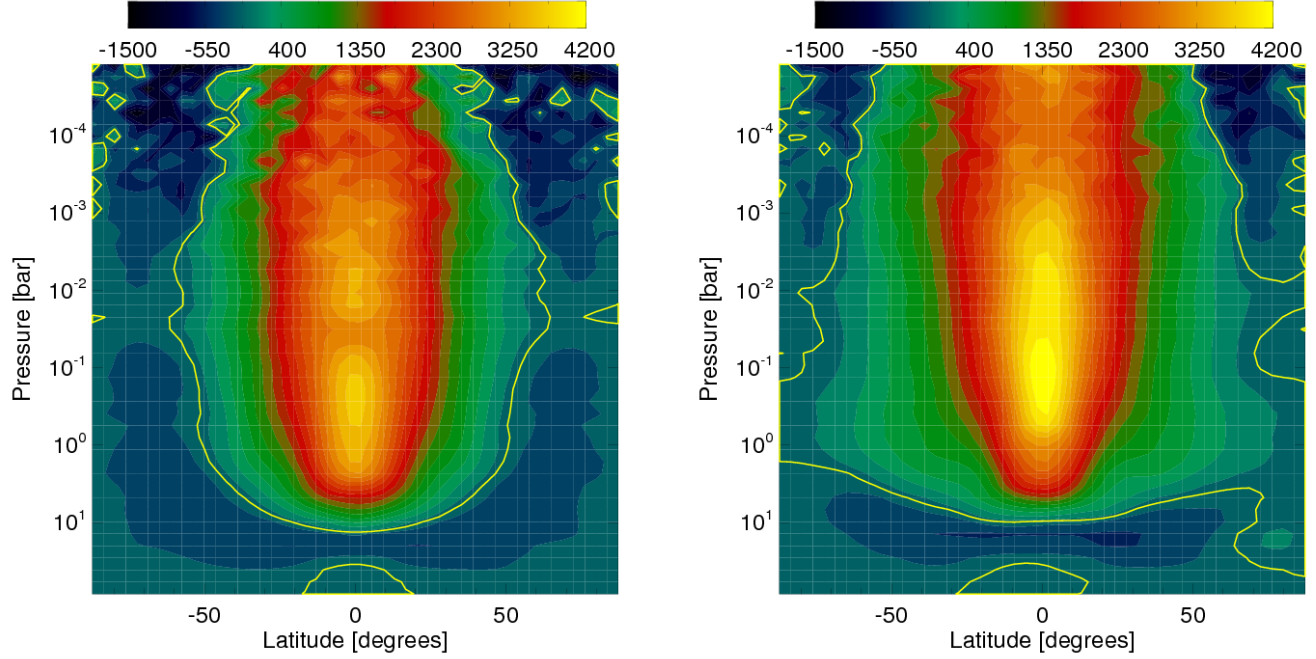
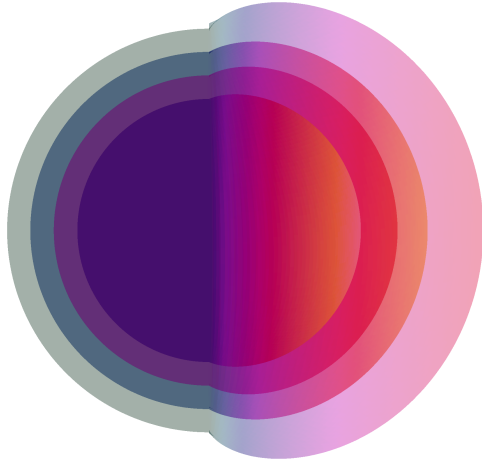
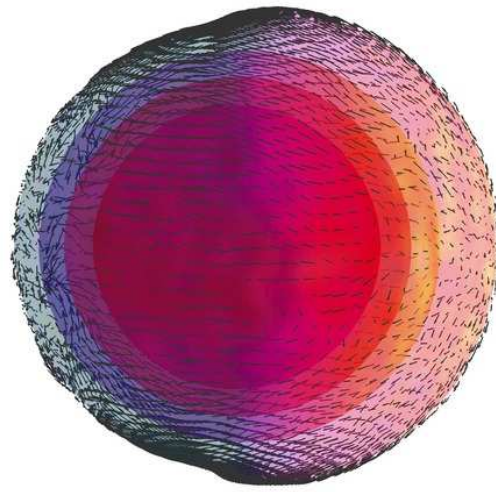


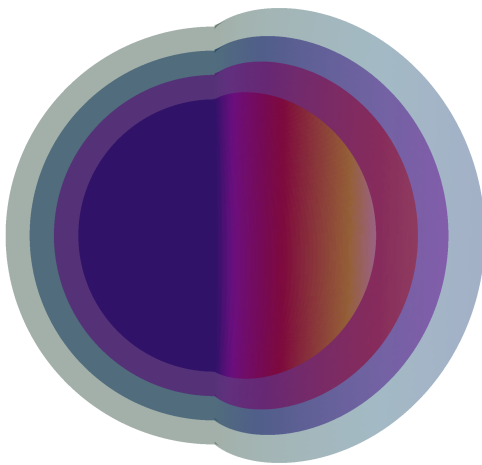
FIG. 2.— The zonal average (i.e., on a latitude circle) of the zonal (east-west) wind in m s^{-1} , as a function of the latitude and pressure level in the atmosphere, for the model with an absorber (left) and the one without (right). The solid yellow lines separate regions of positive (eastward) flow from negative pattern is qualitatively similar in both models. (Also compare to Figure 3 of Rauscher & Menou 2010.)



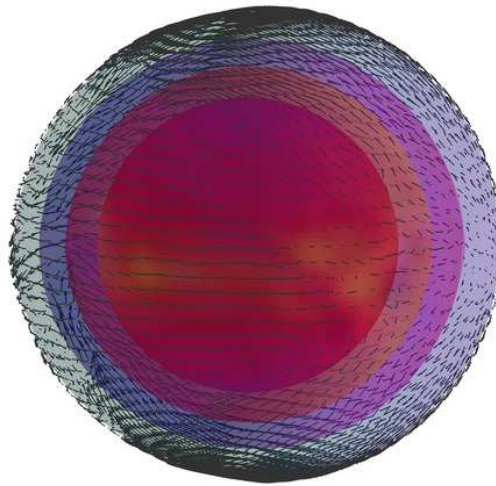
$P = 0.02 \text{ mbar}, 5.7 \text{ mbar}, 0.14 \text{ bar}, 3.6 \text{ bar}$
Central Longitude: -90



$P = 0.02 \text{ mbar}, 5.7 \text{ mbar}, 0.14 \text{ bar}, 3.6 \text{ bar}$
Central Longitude: -90



$P = 0.02 \text{ mbar}, 5.7 \text{ mbar}, 0.14 \text{ bar}, 3.6 \text{ bar}$
Central Longitude: -90



$P = 0.02 \text{ mbar}, 5.7 \text{ mbar}, 0.14 \text{ bar}, 3.6 \text{ bar}$
Central Longitude: -90

FIG. 3.— Temperature maps, with (right) and without (left) dynamical redistribution. The top panels are for the model with an extra optical absorber, and the bottom panels neglect such an absorber. The longitudinal flows distribute heat to the nightside, and thereby partially even out the scale height bulge differential between the dayside and nightside. The vectors on the right-side panels portray the local velocity fields. The vertical scales have been exaggerated by a factor of ten to better visualize the day-night asymmetry. Different pressure levels are shown, at 2.6×10^{-5} , 5.7×10^{-3} , 0.14, and 3.6 bars, and the colors depict the local temperatures on each level. Red is hot and blue is cold.

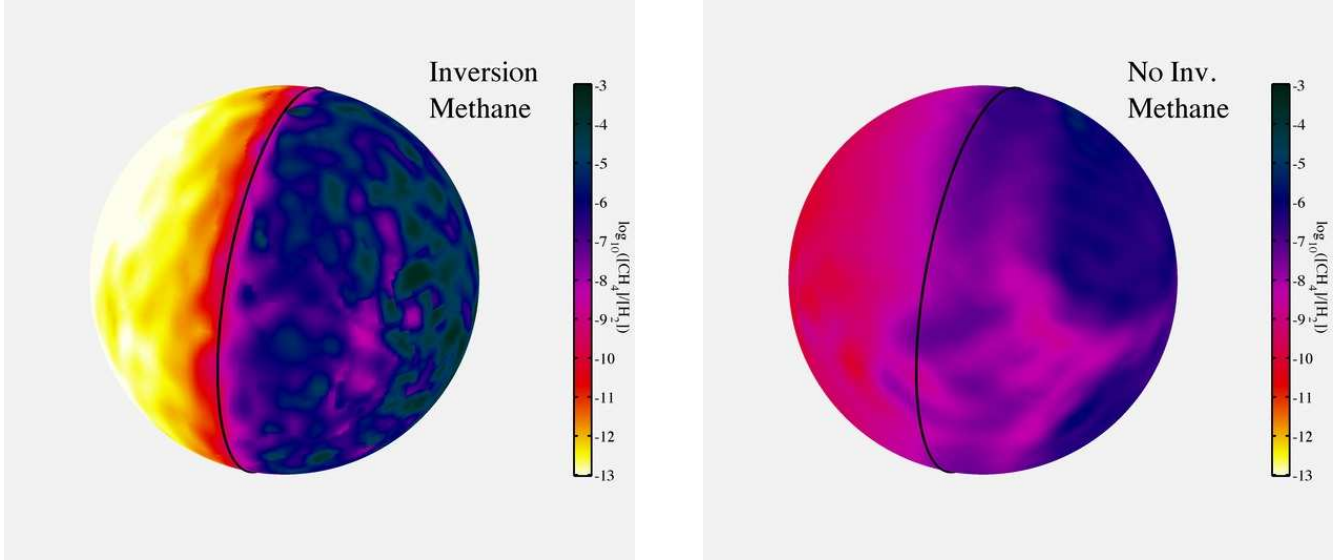


FIG. 4.— These figures depict the distribution of methane (CH_4) over the surface of the 3D GCM models of HD 209458b we are using for this study at a pressure level of 5.7 millibars. Chemical equilibrium is assumed. The left model is with and the right model is without the extra absorber. The nightsides for both are on the right. Reds and yellows indicate low methane abundances and blues and greens represent high methane abundances. If not in methane, carbon would reside in carbon monoxide in these models, which predominates on the daysides (particularly, in this model set, for the model with the extra optical absorber). Color bars indicate the logarithm (base ten) of the methane mixing ratio. The position of the terminator is clearly indicated with a black line. Note on the model without the extra optical absorber (right) the tongue of methane-depleted (CO-rich) material dragged from the dayside to the nightside in the equatorial belt. The degree of such advection is a function of vertical height/pressure level and is greater for the model without the extra absorber.

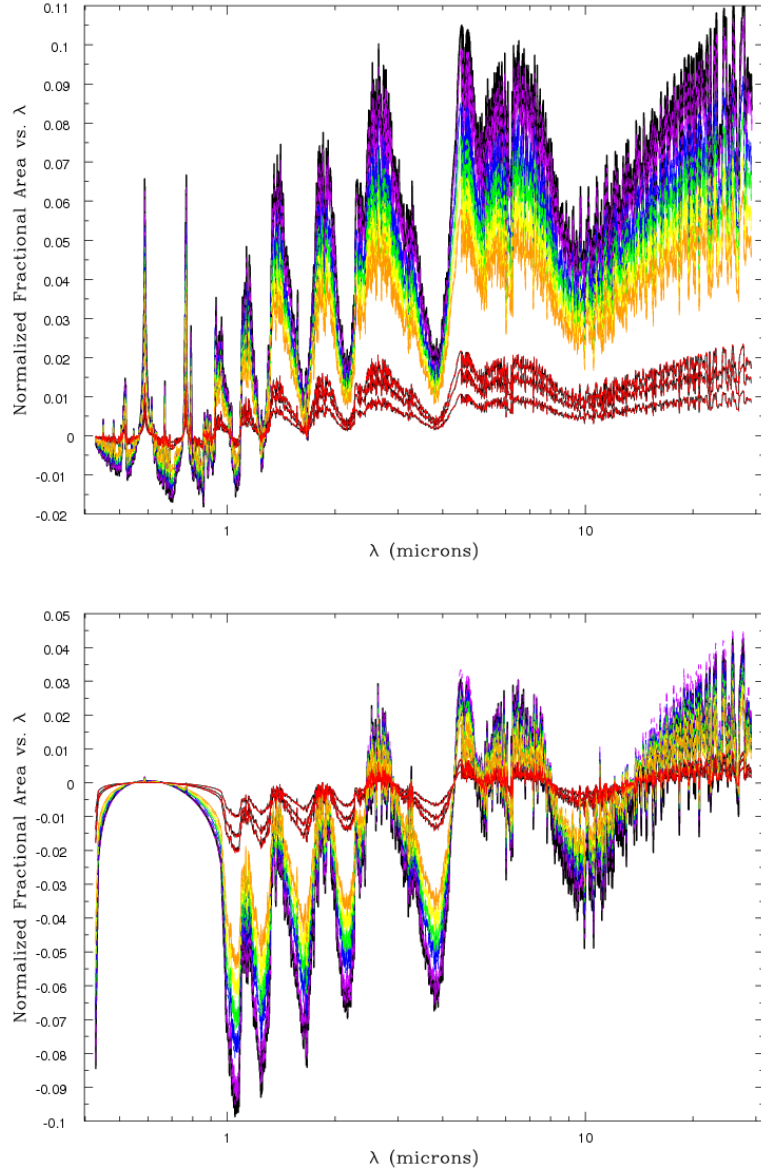


FIG. 5.— **Top:** The normalized fractional area of the atmosphere occulting the star as a function of wavelength (in microns) from the optical to 30 microns as the planet enters and leaves transit. This model is without an extra optical absorber at altitude. The early ingress is depicted in red and the full transit is the upper black curve. The egress is also depicted, but for these models lies very near the ingress lines. The last times of egress are depicted in black and are barely discernible under the corresponding red curves. The times included are -0.063, -0.062, -0.061, -0.053, -0.051, -0.048, -0.047, -0.046, -0.044, +0.046, +0.047, +0.048, +0.051, +0.053, +0.061, +0.062, +0.063 days relative to the time of mid-transit. The fractions are all normalized to the instantaneous average value in the optical wavelength range from 0.5 to 0.7 microns. Hence, the average value of this fraction in that wavelength range (“optical”) is zero. **Bottom:** The same as the top panel, but for the model with the extra absorber at altitude. The action of the extra absorber is clearly seen in the optical region, and the normalization is as performed for the top panel. See text for a discussion.

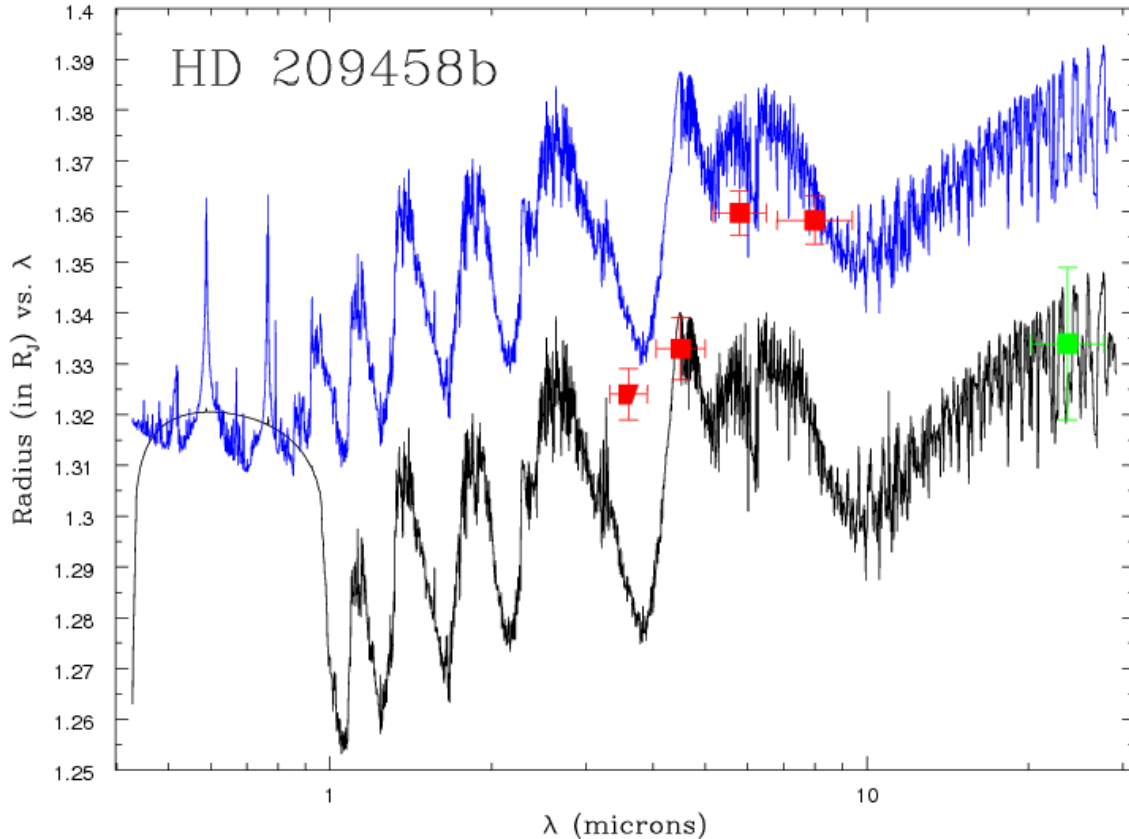


FIG. 6.— A comparison of the transit radii during full transit as a function of wavelength (in microns) for both models depicted in Fig. 3. No limb-darkening corrections are applied. The normalization for both models is to the measured radius in the optical ($\sim 1.32 R_J$; Knutson et al. 2007). Superposed are the transit radius data in the four *Spitzer*/IRAC bands from Beaulieu et al. (2010) and in the 24-micron MIPS band of *Spitzer* from Richardson et al. (2006). See text for a discussion.

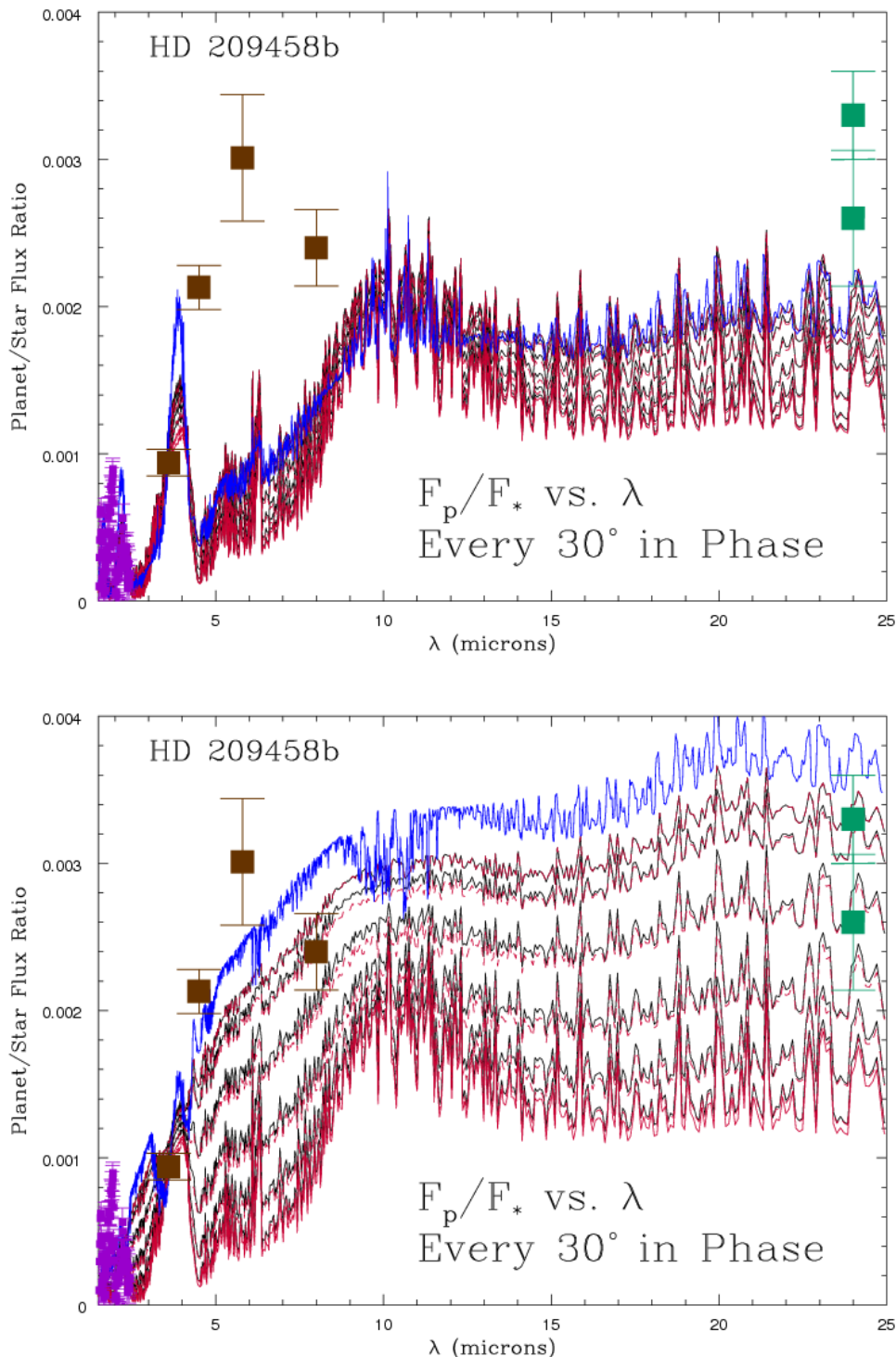


FIG. 7.— Planet-star flux ratios versus wavelength (in microns), for the models with (bottom) and without (top) the extra optical absorber, every 30° in phase of the planet's (HD 209458b's) orbit. Here, zero phase is at secondary eclipse. Superposed are the secondary eclipse data in the *Spitzer*/IRAC (brown) and *Spitzer*/MIPS 24-micron (green) bands from Knutson et al. (2008) and Deming et al. (2005), respectively. The Deming et al. 24-micron data point is accompanied by an additional point (D. Deming, private communication). The $\sim 2\sigma$ difference between these points probably illustrates the systematic uncertainties hidden in these types of measurements. Also included are the Swain et al. (2009) data points between 1.5 and 2.2 microns. The blue lines near the top envelope of each curve set are the corresponding secondary eclipse predictions using the "1D" spectral model method of Burrows et al. (2007,2008b). The red curves are for the first 180° of the orbit and the black curves are for the second. See text for a discussion.

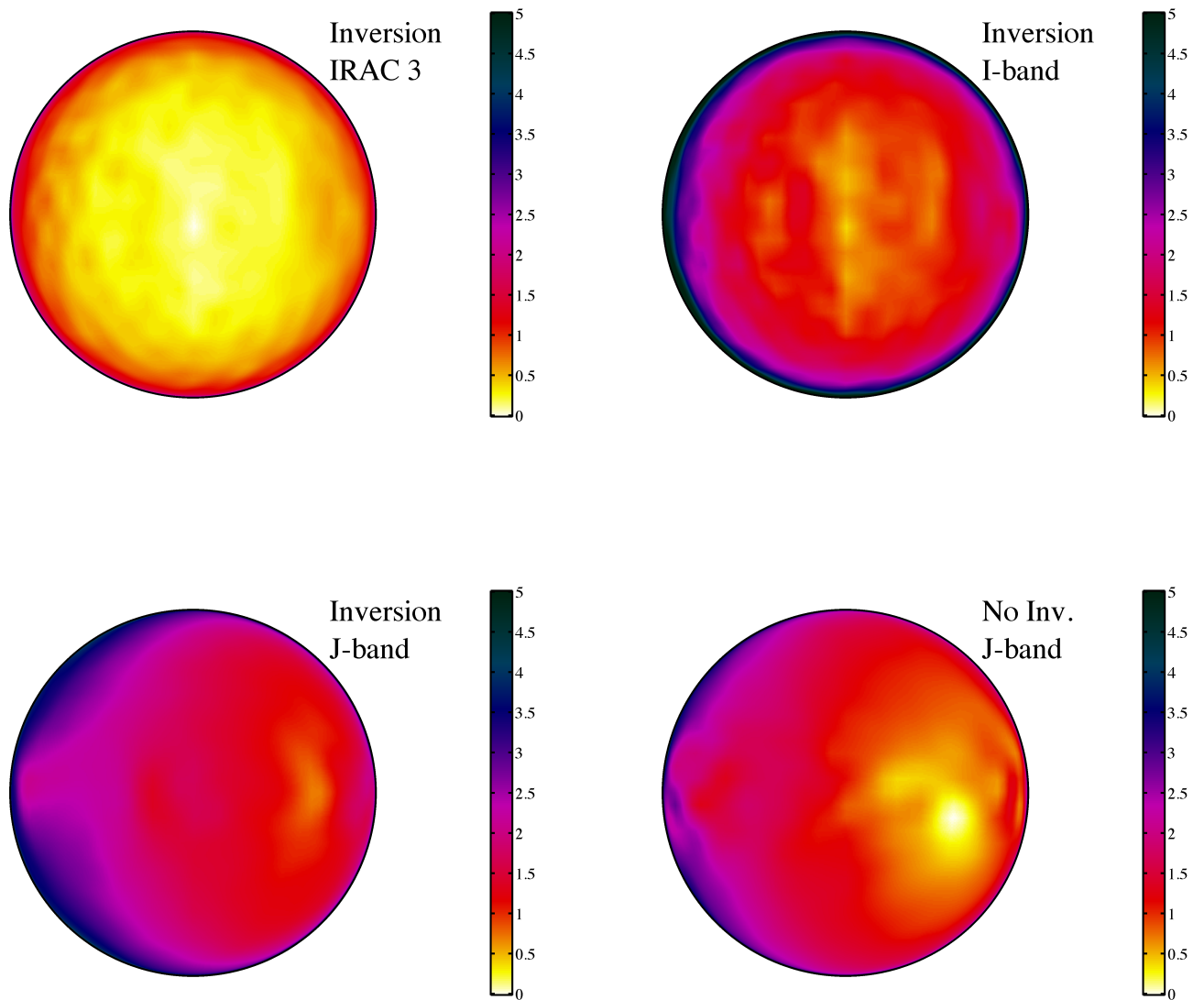


FIG. 8.— These panels are representative planet brightness maps in various wavebands. The top left panel is the IRAC 3 map for the model with an extra absorber; the top right panel is the I band map for the same; the bottom left panel is the J band map for the model with the extra absorber; and the bottom right panel is the corresponding J band map for the model without the extra absorber. All the maps are at full phase (secondary eclipse). The colors and color bars are in relative magnitudes, with the brightest regions rendered in yellow and the dimmest regions in blue. See text for details.

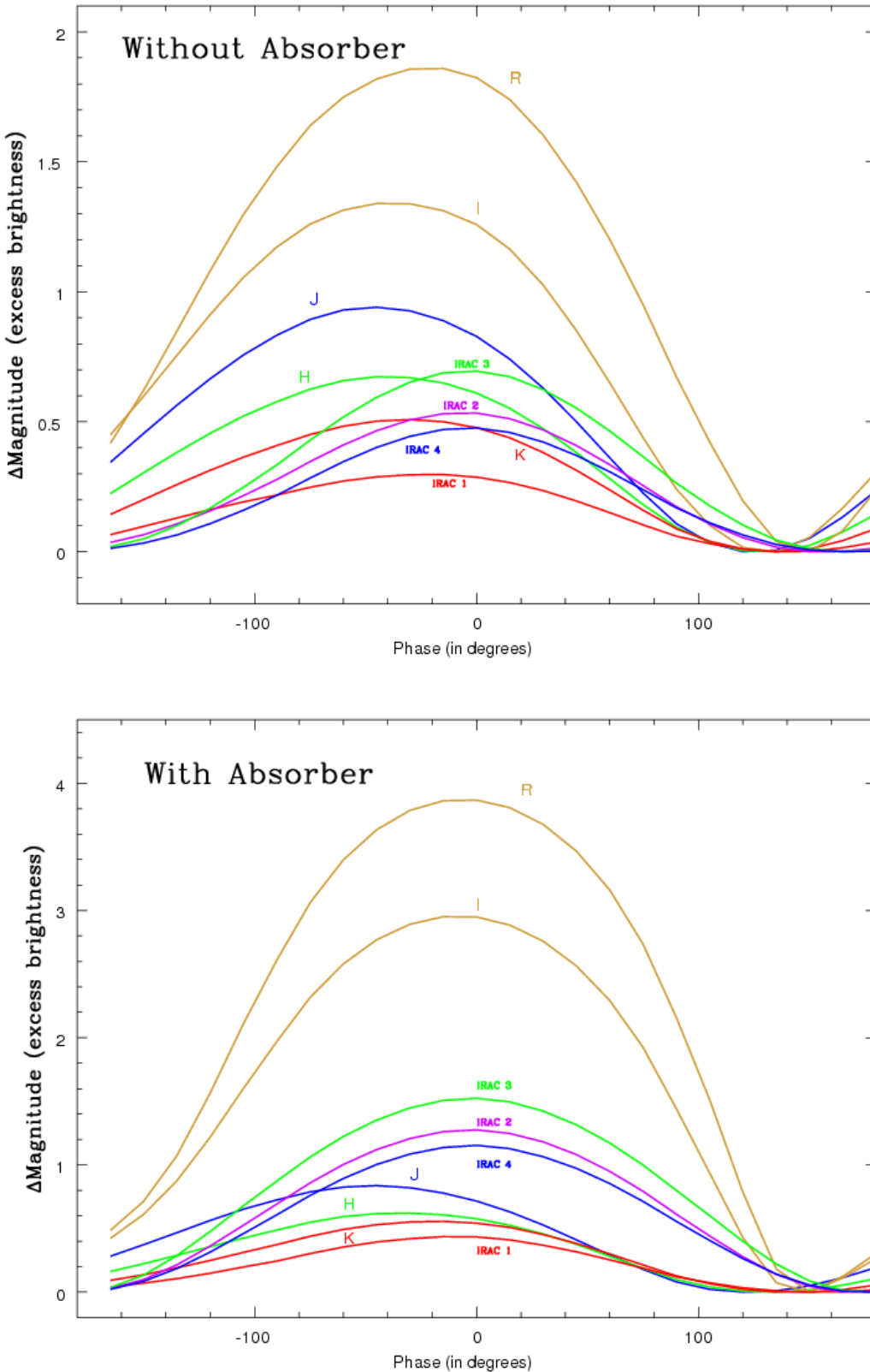


FIG. 9.— The integrated relative light curves (in magnitudes) versus orbital phase in nine different bands (R, I, J, H, K , IRAC 1, IRAC 2, IRAC 3, and IRAC 4) for the models without (top) and with (bottom) an extra optical absorber at altitude and for our fiducial HD 209458b assumptions. These data are derived from integrating maps such as are shown in Figs. 6. The magnitudes are normalized to zero at the dimmest (note !) phases and the magnitude ranges are different for the top and bottom plots. See text for a discussion.